# Dynamic Crack Growth Past a Stiff Inclusion: Optical Investigation of Inclusion Eccentricity and Inclusion-matrix Adhesion Strength

**R. Kitey · H.V. Tippur**

**Abstract** Interactions between a dynamically growing matrix crack and a stationary stiff cylindrical inclusion are studied optically. Test specimens with two different bond strengths (weak and strong) and three crack-inclusion eccentricities ($e=0$, $d/2$ and $3d/4$, $d$ being inclusion diameter) are studied using reflection mode Coherent Gradient Sensing (CGS) and high-speed photography. These variants produce distinct dynamic crack trajectories and failure behaviors. A weaker inclusion-matrix interface attracts a propagating crack while a stronger one deflects the crack away. The former results in a propagating crack lodging ('key-hole') into the inclusion-matrix interface whereas in the latter the crack tends to circumvent the inclusion. When the inclusion is in the prospective crack path, the maximum attained crack speed is much higher in the weakly bonded inclusion cases relative to the strongly bonded counterparts. For a crack propagating towards a weakly bonded inclusion, the effective stress intensity factor ($K_e$) value remains constant for each inclusion eccentricity considered. But these constant $K_e$ values increase with increasing eccentricity. A distinct drop in $K_e$ occurs when the crack is near the inclusion. In strongly bonded inclusion cases, on the other hand, monotonically increasing $K_e$ before the crack reaches the inclusion is observed. A drop in $K_e$ is seen just before the crack reaches the inclusion. The mode-mixity estimates are of opposite signs for weakly and strongly bonded inclusions in case of the largest eccentricity studied, confirming the observed crack attraction and deflection mechanisms.

**Keywords** Dynamic fracture · Crack-inclusion interaction · Optical interferometry · Filled polymers · Toughening mechanisms

## Introduction

Particulate Polymer Composites (PPC) are used in a variety of engineering applications as structural composites, electrically conducting and self-healing adhesives, biocompatible cements, syntactic foams, underfills in electronic packages and so on. Accordingly, there is considerable interest to understand mechanical integrity and failure behaviors of these multiphase materials [1–10]. Previous works suggest that besides the filler volume fraction, filler particle size, size distribution, shape, filler-matrix interfacial strength, also affect the mechanical characteristics of a PPC in general and the fracture behavior in particular. Recent investigations by the authors [11, 12] have revealed that from the perspective of dynamic fracture, a PPC with weakly bonded filler shows higher steady-state fracture toughness when compared to the ones that are strongly bonded at the same (10%) volume fraction and particle size. Combined macro scale interferometric measurements and fracture surface morphology studies suggest increased crack path tortuosity in the former and hence higher effective fracture toughness. This motivates a basic investigation to understand the mechanics of interaction between a dynamically propagating crack and an isolated inclusion as a function of the inclusion-matrix interfacial strength and the

R. Kitey · H.V. Tippur (✉, SEM member)
Department of Mechanical Engineering, Auburn University,
Auburn, AL 36849, USA
e-mail: htippur@eng.auburn.edu

R. Kitey
University of Illinois at Urbana-Champaign
Urbana, IL, USA

inclusion location. This article presents experimental observations on the crack growth behavior in the vicinity of a stiff inclusion embedded in a compliant matrix when the inclusion-matrix interfacial strength is altered between uncoated (weak) to silane coated (strong) states.

Several previous works have used analytical and numerical approaches to examine crack-inclusion interactions under quasi-static loading conditions. Early analytical works of Tamate [13] used 2D complex potentials to study effects of circular inclusions of different elastic characteristics on the stress state and stress intensity factors near mode-I cracks. The stress field near a crack-tip when an inclusion is symmetrically located in front of it is examined by Atkinson [14]. He has concluded that an inverse $\sqrt{r}$ variation prevails even when the crack is at small distances from the inclusion. Erdogan et al. [15] examined stress fields and evaluated stress intensity factors for arbitrarily oriented cracks with respect to circular inhomogeneities using Green's functions approach. Stable crack growth behavior in the presence of a circular inclusion near a crack is studied using the strain energy density theory by Gdoutos [16]. Crack-inclusion positions, mechanical properties and crack length are among the parameters examined in this work. Li and Chudnovsky [17] examined effects of an elastic inclusion on the energy release rate associated with crack extension. They showed that when a crack in an elastic material approaches a rigid inclusion, the crack-tip is shielded from the far field stresses but as the crack propagates past the inclusion the stresses amplify. Using boundary element method, Bush [18] investigated the effect of a single inclusion and an inclusion cluster on the crack trajectory and crack driving force. Situations of fully and partially bonded inclusions are studied in this work. Knight et al. [19] examined crack deflection/attraction mechanisms associated with crack-particle interactions by parametrically studying different elastic mismatches and an interphase region between the matrix and the inclusion. Using symmetric Galerkin formulations in boundary element method and the maximum tangential stress criterion for crack growth, Kitey et al. [20] simulated two dimensional mixed-mode quasi-static crack growth near perfectly bonded stiff particles and particle-clusters. They observed that the crack driving force is affected much earlier than perceivable crack deflection. Also, they noted that as the eccentricity of the inclusion relative to the crack increases, the energy release rate increases. Among the very few dynamic studies in this area, Lei et al. [21] introduced a boundary element methodology for studying dynamic interaction between a moving crack in an elastic medium with an inclusion. Results on crack path, crack speed and dynamic stress intensity factor histories are obtained by invoking crack growth criteria during crack-inclusion interaction.

Despite being a problem of fundamental interest for modeling fracture and failure of many practical heterogeneous materials systems, surprisingly very few experimental studies are reported in the literature on this topic. Further, the ones reported are carried out under quasi-static conditions. O'Toole and Santare [22] are among the exceptions who have investigated crack-inclusion interactions experimentally. They used photoelasticity to study a perfectly bonded inclusion in an elastic matrix. Two identical steel inclusions on the two opposite faces of a thin polycarbonate plate are used to simulate an inclusion. They studied the influence of elliptical inclusions on an edge crack in an elastic medium. Another interesting experimental study in this regard is reported by Li and Chudnovsky [17]. They modeled perfectly bonded second phase inclusion in a matrix by altering the chemical structure of a polymer by selectively exposing to UV radiation. They experimentally measured crack speed in fatigue loaded crack-inclusion specimens and qualitatively observed fracture surface morphology.

This paper examines crack growth behavior in the vicinity of an isolated, stiff inclusion using optical interferometry. Of particular interest is the dynamic crack growth that often occurs in brittle polymers under impact and shock loading conditions. Visualization of optical fields representing instantaneous crack-tip deformations and crack paths when (a) the bond strength between the matrix-inclusion pair and, (b) the eccentricity of the inclusion relative to the initial crack are varied is of central interest. The optical fields are analyzed on the initial approach of a dynamically growing crack towards an inclusion to quantify fracture parameters and discern effects of experimental parameters. In the following sections, details of specimen preparation, experimental method used, optical fields mapped during crack-inclusion interactions, analysis of optical fields to extract fracture parameters, are presented.

## Material Preparation and Specimen Geometry

Low viscosity epoxy,[1] prepared by mixing Bisphenol-A resin and Amine based hardener is used as the matrix material. First the resin and the hardener are mixed in the ratio of 100:36. Prior to transferring the mixture to the mold, a cylindrical glass inclusion of diameter $d=4$ mm and length equal to the specimen thickness (8 mm) is positioned at the center of the mold, as shown in Fig. 1. The material is cured at room temperature for about 3 days. (The slow
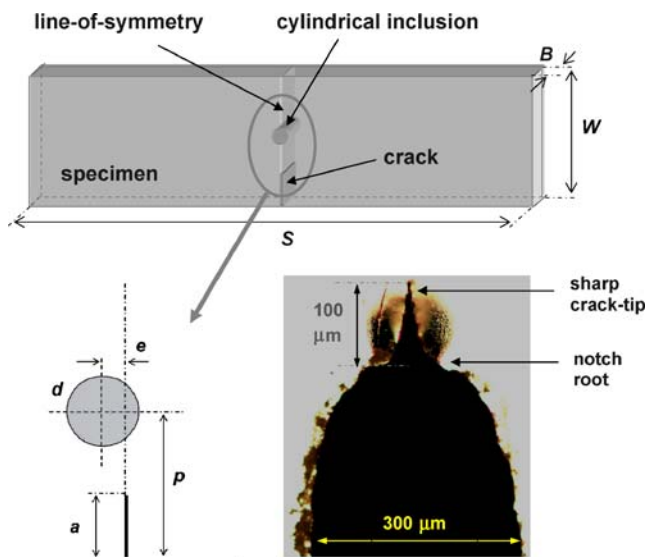
**Fig. 1** Epoxy specimen with cylindrical glass inclusion located in front of initial crack-tip. Inclusion location is defined by $p$, the initial distance of the inclusion center from the specimen edge which contains the crack and the eccentricity $e$, the distance between the inclusion center and the line-of-symmetry. $p=20$ mm, $d=4$ mm, $S=140$ mm, $W=42$ mm, $B=8$ mm, $a=5$ mm. Sharp crack tip created by forcing a razor blade into the notch root is also shown

curing at room temperature helps reduce residual stresses.) To create a weak inclusion-matrix interface an uncoated (untreated) inclusion is used. A strong inclusion-matrix adhesion is achieved using Amino Silane coating, γ-aminopropyltrimethoxysilane ($H_2NC_2H_4NHC_3H_6Si(OCH_3)_3$) (specific gravity 1.02 at 25°C), on the inclusion as an adhesion promoter between the inclusion and matrix material.[2]

The cured sheets are machined into test specimens of dimensions 152 mm×42 mm×8 mm as shown in Fig. 1. The specimen surface is then polished with #150 grit sand paper and cleaned. The surface is then made optically flat and specular by transferring an aluminum film (a few nm thick) using a coated optical flat and a layer of epoxy. The aluminum film is first deposited on an optically flat borosilicate glass window of ~50 mm diameter. A layer of liquid epoxy is then sandwiched between the roughened specimen and the face of the optical flat deposited with aluminum film. The reflective film gets transferred to the specimen upon curing of the epoxy layer due to higher bond strength between epoxy and aluminum compared to the one between aluminum and glass. An edge notch of 150 μm root radius and 5 mm nominal length ($a$) is cut into the specimen using a high-speed diamond impregnated circular saw. Further, a sharp crack-tip is created by pressing a sharp razor blade into the notch root. A

---

[2] In a companion quasi-static investigation it is determined that nominal interfacial strength of an uncoated glass/epoxy interface is 3±1 MPa while for a silane treated one it is 9±1 MPa.

microscopic image of the sharp crack-tip is also shown in Fig. 1. A relatively dark region around the initial notch tip indicates permanent deformation due to compressive stresses generated when the razor blade is pressed into the notch root. A virtual line from the initial crack-tip in the loading direction is referred to as the *line-of-symmetry*. The location of the inclusion in the specimen relative to the crack-tip is identified by two parameters; ($p$-$a$) and $e$ (see Fig. 1). The distance of the inclusion center from the specimen edge with the crack of length $a$ is defined by $p$. The eccentricity, $e$, is defined as the distance between the inclusion center and the line-of-symmetry. In the current study, three different eccentricities, $e=0$, $d/2$ and $3d/4$ are considered, and $p=20$ mm is maintained constant in all experiments.

## Experimental Set-up

The optical method of Coherent Gradient Sensing (CGS) is used to investigate interaction of a growing crack in epoxy with an isolated glass inclusion. CGS measures surface slopes when used in the reflection mode. The schematic of the experimental set-up for reflection CGS [23, 24] employed is shown in Fig. 2. A collimated beam of coherent laser light illuminates an opaque specimen with a specularly reflective surface. The reflected object wave front is incident on a pair of high-density Ronchi gratings $G_1$ and $G_2$, spatially separated by a distance $\Delta$, as shown. These gratings diffract the object wave-front successively in several discrete directions. The filtering lens L collects the light field and displays its frequency content on its back focal plane as a series of diffraction spots. By locating a filtering aperture around ±1 diffraction order on the focal plane, the information about surface slopes in the form of interference fringes is captured at the image plane. The imaging system (lens+image plane) is kept focused on the object surface.

The experimental set-up includes a pneumatic hammer, a pulse laser, CGS interferometer and a continuous access high-speed camera. An Argon-ion pulse laser beam (wave length λ=514 nm) is expanded and collimated into a 50 mm diameter beam. A pneumatic hammer with a hemispherical tip is used to impact (velocity 5.3 m/s) the center of the specimen along the $x$-axis, as shown in Fig. 2. The specimen is initially rested on two soft-putty blocks to simulate 'free–free' supports. Before the impactor contacts the specimen, a flag triggers a photo-detector which in turn opens a capping shutter located in front of the camera lens. This allows the laser beam to expose a strip of photographic film pre-positioned in a circular track in the camera. As soon as the impactor touches an adhesive backed copper tape affixed to the top edge of the specimen, an electric

**Fig. 2** Experimental set-up for coherent gradient sensing (CGS)
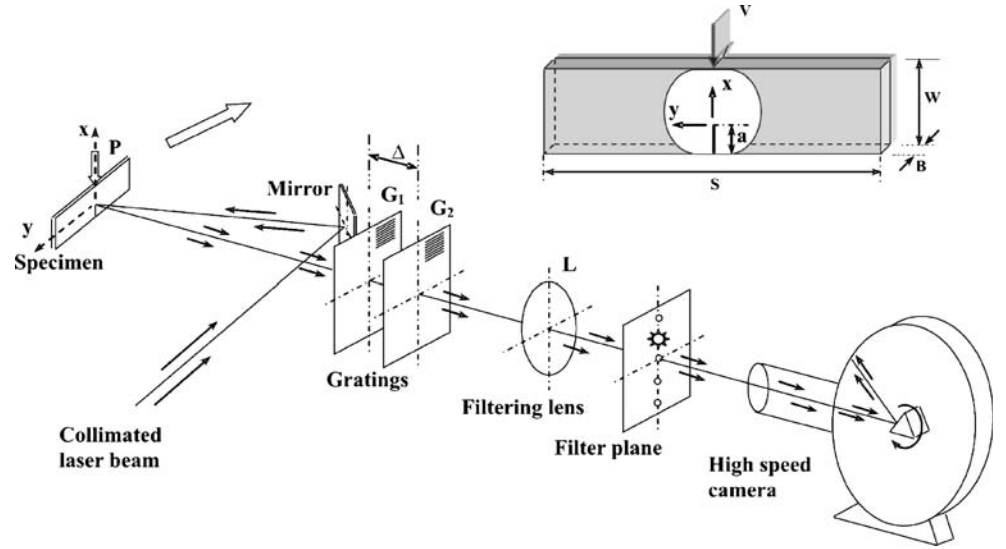


circuit is closed to initiate a gate pulse of 320 μs duration. Laser pulses of 50 ns width are repeated at 5 μs intervals (200,000 fps) during the gate period. With these settings, approximately 70 images are exposed onto the photographic film. The incident beam reflecting from the deformed surface carries information about the local non-planarity of the surface near the points of interest, the crack tip, the inclusion and the impact point. The angular deflections of light rays relative to the optical axis are measured as interference fringes. The fringe patterns representing contours of $\partial w/\partial x$ where $w$ is the out-of-plane displacement and $x$ is the direction of the initial crack orientation are recorded. The governing equation for reflection mode CGS is,

$$\frac{\partial w}{\partial x} = N \frac{p_g}{2\Delta}, \quad N = 0, \pm1, \pm2, \ldots, \quad (1)$$

where $N$ denotes fringe orders, $p_g$ is the grating pitch (25 μm) and $\Delta$ is the gratings separation distance (48 mm).

Crack Velocity and Stress Intensity Factor Evaluation

The instantaneous values of crack length are measured by locating the crack-tip from the digitized interferograms. From the crack length histories, crack speed ($V$) is calculated as,

$$V = \left(\frac{da}{dt}\right)_i = \frac{a_{i+1} - a_{i-1}}{t_{i+1} - t_{i-1}}, \quad (2)$$

where $a_i$ and $t_i$ denote instantaneous crack length and time instants, respectively.

Interferograms are also used to quantify instantaneous fracture parameters by digitizing optical information around the crack-tip to obtain fringe location, $(r,\theta)$, and fringe order, $N$, data. The governing equations to extract mixed-mode (mode-I and mode-II) stress intensity factors for a linear elastic asymptotic stress field in the vicinity of a steadily propagating crack are given by [25],

$$w = -\frac{\nu B}{(1+\nu)(1-2\nu)}$$

$$\left[ r_l^{-1/2} \left\{ A_0 \cos\frac{\theta_l}{2} - B_0 \sin\frac{\theta_l}{2} \right\} + r_l^0 A_1 + r_l^{1/2} \left\{ A_2 \cos\frac{\theta_l}{2} + B_2 \sin\frac{\theta_l}{2} \right\} + O(r) \right] \quad (3)$$

where

$$A_0 = \frac{(1-\alpha_s^2)(1-\alpha_l^2)}{4\alpha_s\alpha_l-(1+\alpha_s^2)^2} \frac{K_I}{\mu\sqrt{2\pi}}, \quad B_0 = \frac{2\alpha_s^2(1-\alpha_l^2)}{4\alpha_s\alpha_l-(1+\alpha_s^2)^2} \frac{K_{II}}{\mu\sqrt{2\pi}},$$

$$r_l = r\cos\theta(1 + \alpha_l\tan^2\theta), \quad \theta_l = \tan^{-1}(\alpha_l\tan\theta),$$

$$\alpha_{l:s} = \sqrt{1 - \left(\frac{V}{C_{l:s}}\right)^2},$$

$r$ and $\theta$ are the polar coordinates defined at the current crack-tip, $A$s and $B$s are coefficients of the asymptotic series and $C_1$ and $C_s$ are longitudinal and shear wave speeds. The above can also be used for analyzing pre-initiation interferograms by setting $V \rightarrow 0$ which reduces the equations to the case of a dynamically loaded stationary crack. The digitized data are used in the above equation in conjunction with overdeterministic least-squares analysis (see, [11] for details) to evaluate mode-I and mode-II stress intensity factors. Further, $K_I$ and $K_{II}$ are used to calculate an effective stress intensity factor, $K_e$, and phase angle, $\psi$, as,

$$K_e = \sqrt{K_I^2 + K_{II}^2}, \quad \psi = \tan^{-1}\left(\frac{K_{II}}{K_I}\right) \quad (4)$$

The region of dominant 3-D effects in the vicinity of the crack-tip $r/B<0.5$ is excluded from the analysis to estimate SIFs. Also, only the data behind the crack $90°\leq\theta\leq150°$ is considered since it has been demonstrated that triaxial effects are minimum in this region [26] for the field under consideration. Since the measured data used in the analysis

comes from a region beyond $r/B=0.5$, considering non-singular terms in the least-squares analysis is necessary to account for far-field stresses. It has been found that by including the first three terms of the asymptotic stress field, $K_e$ can be evaluated accurately [11]. It should be noted that equation (3) is used to obtain instantaneous fracture parameters until the crack reaches the inclusion-matrix interface. Large perturbations to crack-tip fringes as crack-inclusion interaction occurs make fringe analysis quite challenging. Further, the effective stress intensity factor decreases due to asperities in the mating fracture surfaces (see [27, 28]) and the analysis of the same is also not attempted in current work.

### Qualitative Analysis of Interferograms

The interference fringes recorded during experiments for weakly and strongly bonded inclusions of various eccentricities are analyzed qualitatively in this section.

Weakly Bonded Inclusion ($e=0$)

Optical interference fringes shown in Fig. 3 are obtained for an epoxy specimen with a symmetrically located ($e=0$) weakly bonded inclusion. The time designated on each image is the time instant after the impact. The first image at 70 μs corresponds to the one from the pre crack initiation period. Interference fringes at both the impact point and the crack-tip can be seen in each image. Fringe lobes on the top and bottom of the inclusion can also be noticed due to material discontinuity at the inclusion-matrix interface. Both the impact point and the crack-tip fringes evolve in size with time. In this experiment, the crack initiates at ∼105 μs (interferogram not shown). The next image at 135 μs shows the crack propagating towards the inclusion. A sharp crack-tip used in the experiment results in a smooth crack initiation event without perturbing the crack-tip fringes visibly. (This is unlike a highly transient initiation often seen when a blunt notch is used [11]. A gradual initiation is important to the current investigation because crack initiation dynamics are less important when compared to the ones due to crack-inclusion interaction.) Symmetry of interference fringes relative to the crack plane suggests a mode-I fracture event. As the crack approaches the inclusion, front lobes of the symmetric 'tri-lobed' pattern interacts with the inclusion before merging into the inclusion-matrix interface. The rear lobes, however, seem relatively unperturbed during this time. In the vicinity of the inclusion, the size of fringe lobes behind the crack-tip visibly shrinks indicating lowering of crack-tip stress intensity. Also, the propagating crack slows down during
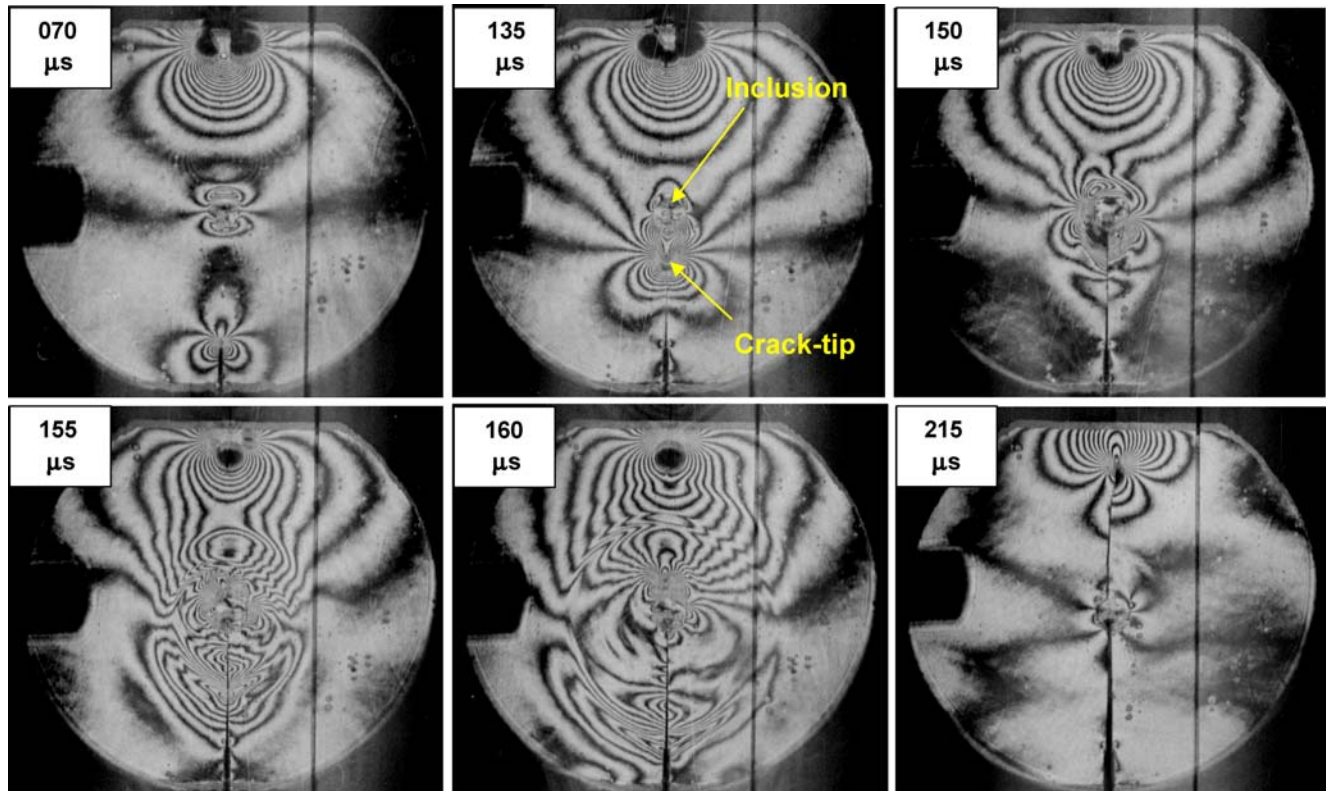


**Fig. 3** Selected fringe pattern representing surface slope contours $\partial w/\partial x$ for epoxy specimen with weakly bonded inclusion located symmetrically ($e=0$) with respect to the initial crack-tip. (Distance between the crack and the vertical line is 10 mm.)

these time instants (interferogram not shown). The crack interaction with the inclusion at instants 150, 155 and 160 μs show a large disturbance in the crack-tip fringes. Some degree of perturbation in fringes can be noticed near the inclusion-matrix interface at 150 μs, which evolves into an arrest wave in the next few images. The reinitiation wave also can be seen in the next two images at 155 and 160 μs time instants. In these images, there is evidence of branching of interfacial debond front into two paths, one of which is ahead of the other. In the subsequent frames the tip which is ahead of the other continues to grow successfully while the other stalls.

The arrest and reinitiation waves are better visible in the enlarged interferogram at 160 μsec time instant shown in Fig. 4. The advancing and the stalled crack-tips are marked separately on either sides of the inclusion on the inclusion-matrix interface. It should also be noted that during crack arrest and reinitiation multiple waves emerge from the inclusion-matrix interface. Collectively these waves are represented by the dotted lines in the figure. Broadly, two different waves are discernible. First, an arrest wave, centered approximately at the point where the crack first meets the inclusion and the second, a reinitiation wave, centered at the point on the inclusion-matrix interface from where the crack reinitiates. Nearly the same size (radii) of

the arrest and the reinitiation waves, with the latter being slightly smaller than the former, suggests that due to a weak inclusion-matrix interface reinitiation takes place almost instantaneously after the crack first encounters the inclusion. From time lapse calculations, both arrest and reinitiation waves are found to be traveling at a velocity of ~950 m/s, close to the value of the Rayleigh wave speed for epoxy. The temporal resolution used in this work (5 μs interframe time) seems insufficient to capture all the details of debond dynamics and is deferred to a later investigation.

At 215 μs (see Fig. 3) both the debonded inclusion and the reinitiated crack are clearly visible. A photograph of the fractured specimen from this experiment is shown in Fig. 5(a). The vertical arrow indicates the direction of crack propagation whereas a dotted circle highlights the inclusion. The debonding of the inclusion and the location where the crack reinitiates is clearly visible in the image. The crack has reinitiated in a mode-I fashion from the inclusion-matrix interface and with nearly zero offset distance relative to the initial crack path.

Strongly Bonded Inclusion ($e=0$)

The set of fringes shown in Fig. 6 is from a specimen with a symmetrically located ($e=0$) inclusion bonded strongly to



Fig. 4 Stress waves due to crack-inclusion interaction when the inclusion is weakly bonded to the matrix. Trace of kinks in fringes suggests arrest and reinitiation waves
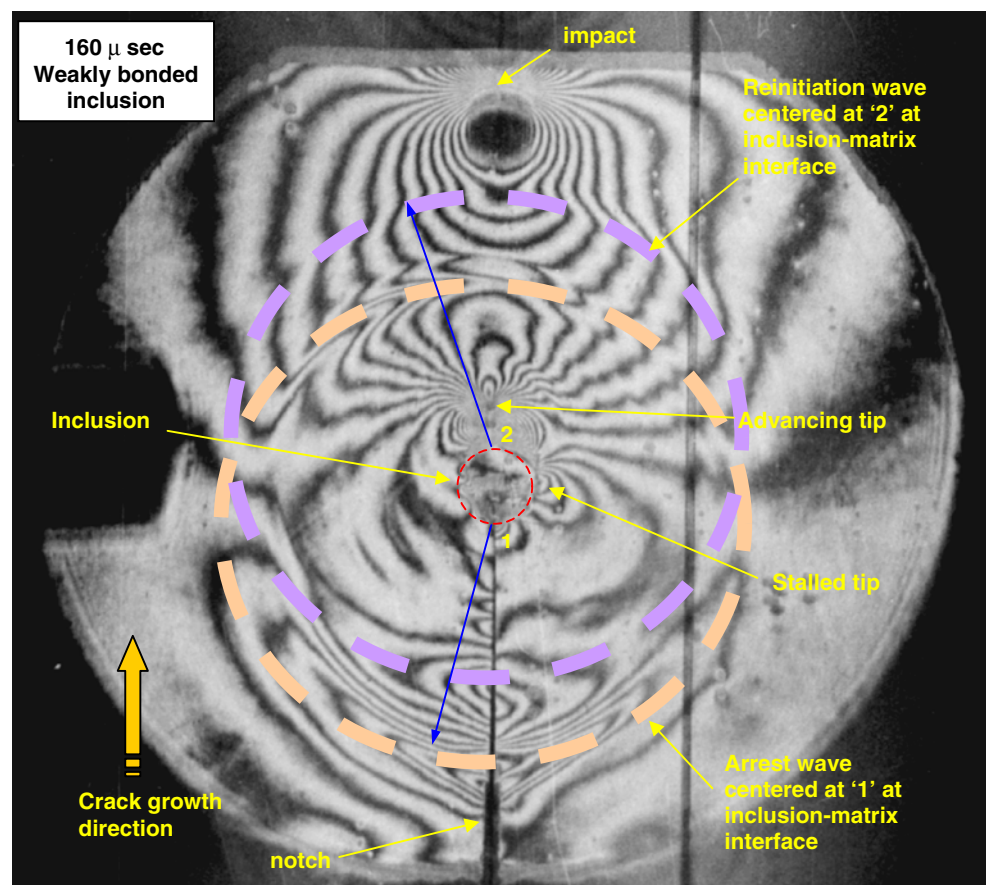
**Fig. 5** Images of fractured specimens showing differences in crack-inclusion interaction: (**a**) symmetrically located (*e*=0) weakly bonded inclusion, (**b**) symmetrically located (*e*=0) strongly bonded inclusion, (**c**) tangentially located (*e*=*d*/2) weakly bonded inclusion, (**d**) tangentially located (*e*=*d*/2) strongly bonded inclusion, (**e**) weakly bonded inclusion at *e*=3*d*/4, (**f**) strongly bonded inclusion at *e*=3*d*/4 (*Arrow* indicates crack growth direction.)
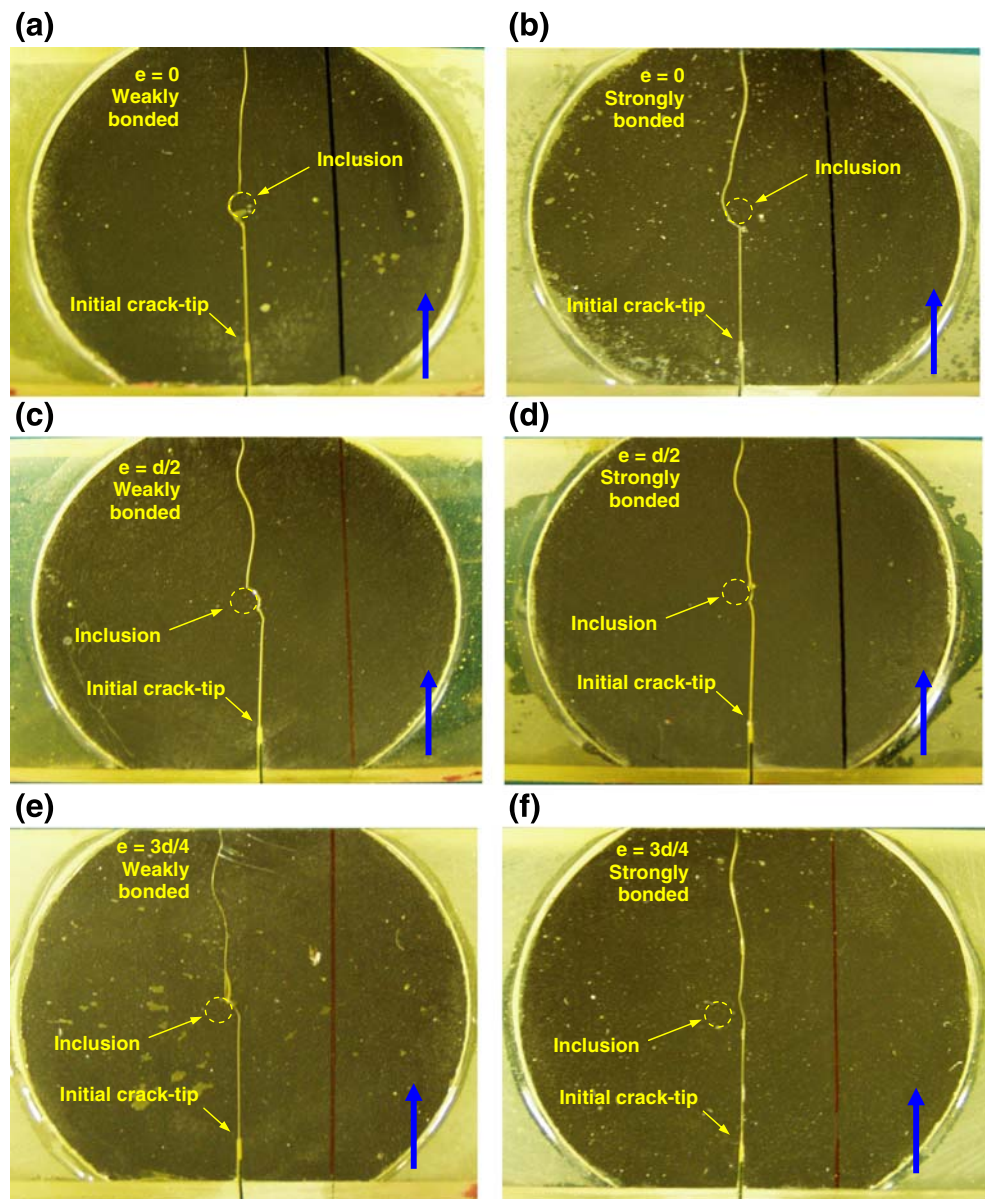


the matrix. The first image at 65 μs is from the pre-initiation period. The crack initiation (interferogram not shown) in this case is observed at 115 μs. Next image at 140 μs time instant shows front fringe lobes at the crack-tip interacting with the inclusion as it is being approached. The perturbation in crack-tip fringes at 155 μs is noticeable as the crack meets up with the inclusion-matrix interface. This generates an arrest and a reinitiation wave from inclusion-matrix interface. These two waves are clearly visible in the next two images at 160 and 165 μs. In these, crack front branching into a successfully advancing tip and a stalled tip is also evident.

In Fig. 7 an enlarged interferogram at 165 μs time instant shows multiple stress waves due to crack-inclusion interaction. A distinct difference in emanating stress waves can be noticed when Figs. 4 and 7 are compared for the weakly and strongly bonded inclusion cases, respectively. Unlike in case of the weakly bonded inclusion, it is more difficult to distinguish the arrest wave from the reinitiation wave in case of strongly bonded inclusion because both waves have nearly the same center of origin at a point where the crack first meets the inclusion.

The interferogram at time instants from 215 μs in Fig. 6 shows the crack propagating away from the inclusion. This also shows the reinitiation to have occurred at a tangential location on/near the inclusion-matrix interface and subsequently propagating at an angle towards the impact point. The shrinking crack-tip fringes suggest lower stress intensity as the crack approaches the impact point. The crack deflection and propagation around a strongly bonded inclusion can be seen in Fig. 5(b). This is unlike the weakly bonded case where the inclusion-matrix interface debonds
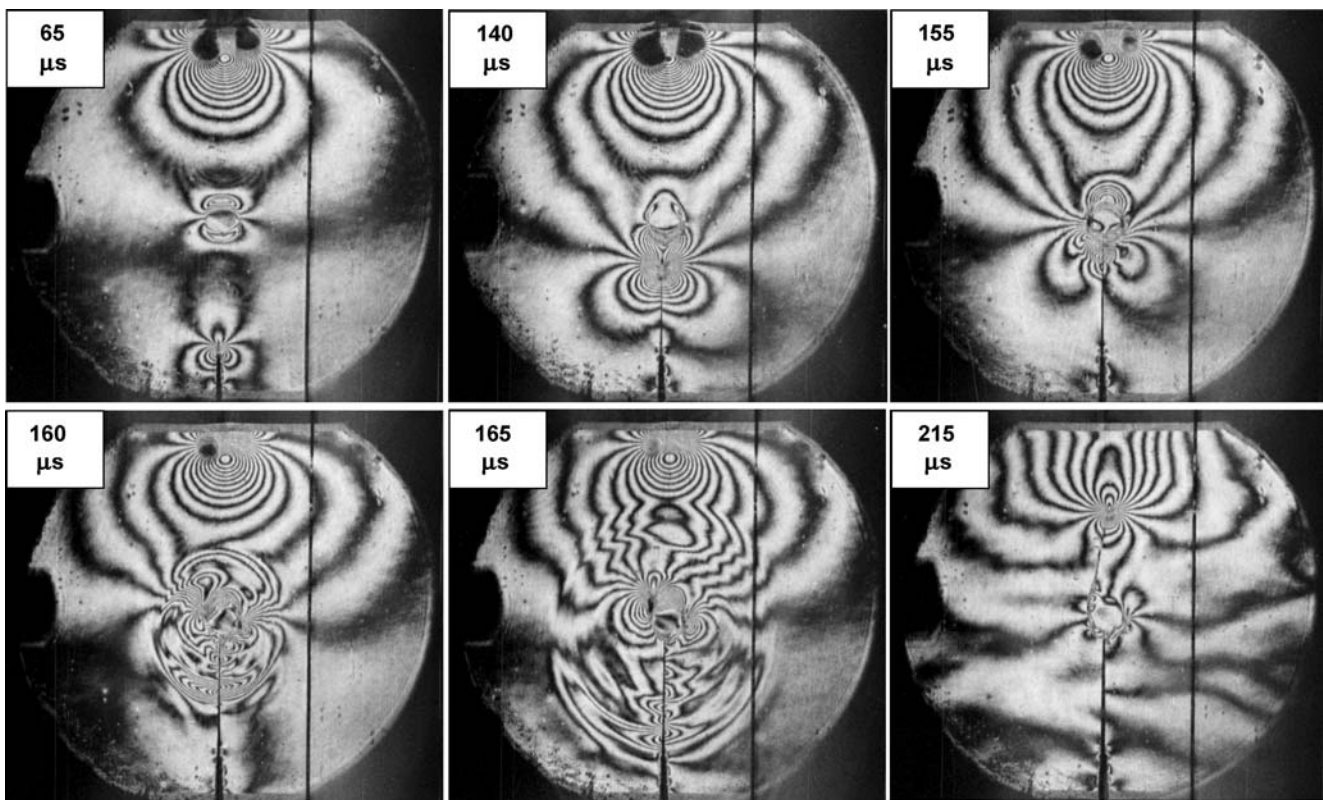
**Fig. 6** Selected fringe pattern representing surface slope contours $\partial w/\partial x$ for epoxy specimen with strongly bonded inclusion located symmetrically ($e=0$) with respect to the initial crack-tip. (Vertical line is at 10 mm distance from the initial crack line.)

and the crack lodges into the interfacial cavity before reinitiating.

### Weakly and Strongly Bonded Inclusions ($e=d/2$)

Experiments are also performed with inclusions initially located with an offset distance relative to the initial crack. The crack in this case is initially oriented tangentially to the inclusion boundary ($e=d/2$). Figure 8 shows a few selected interferograms for weakly (top row) and strongly (bottom row) bonded inclusion cases. For brevity only three interferograms, all from the post-crack initiation regime, are shown.

The first image at a time instant of 125 μs in Fig. 8(a) for the specimen with a weakly bonded inclusion shows crack propagating towards the inclusion (the dark spot in front of the tip is due to unavoidable mirror-face-switching in the high-speed camera). The front lobes of the crack-tip fringes interacting with the inclusion can be seen. Next image at 145 μs shows a reinitiated crack-tip at the inclusion-matrix interface and centered at a point shifted to the left of its original track. This interferogram also shows evidence of an arrest wave seen as a circular perturbation in an otherwise smooth field of fringes as distinct kinks. The path of the crack in the region past the inclusion is evident in the third

image at 165 μs. The shifted crack paths are clear in this frame. The corresponding fractured specimen photograph is shown in Fig. 5(c).

Figure 8(b) shows interferograms for a specimen with strongly bonded inclusion. The first image in this row at 150 μs shows the crack-tip fringes interacting with the inclusion when the crack is about to reach the inclusion. A relatively mild stress wave emerging from the inclusion-matrix interface can be noticed from the next image at 160 μs as the crack grazes past the inclusion propagating tangentially to it. This is visible in the third image at 190 μs where the crack has propagated past the inclusion sufficiently. The corresponding photograph of the fractured specimen is shown in Fig. 5(d).

### Weakly and Strongly Bonded Inclusions ($e=3d/4$)

The crack-inclusion interaction for the specimen with inclusion at an offset distance of $e=3d/4$ shows features similar to the one for $e=d/2$. Therefore a detailed description is avoided here for brevity. The prominent difference, however, can be noticed in the crack paths shown in Fig. 5. The crack path for the weakly bonded inclusion case is shown in Fig. 5(e). Even though the inclusion is not in the prospective crack path, crack is clearly attracted towards the weaker (or, weakened)

**Fig. 7** Stress waves due to crack-inclusion interaction when the inclusion is strongly bonded to the matrix. Traces of kinks in fringes suggest arrest and reinitiation waves
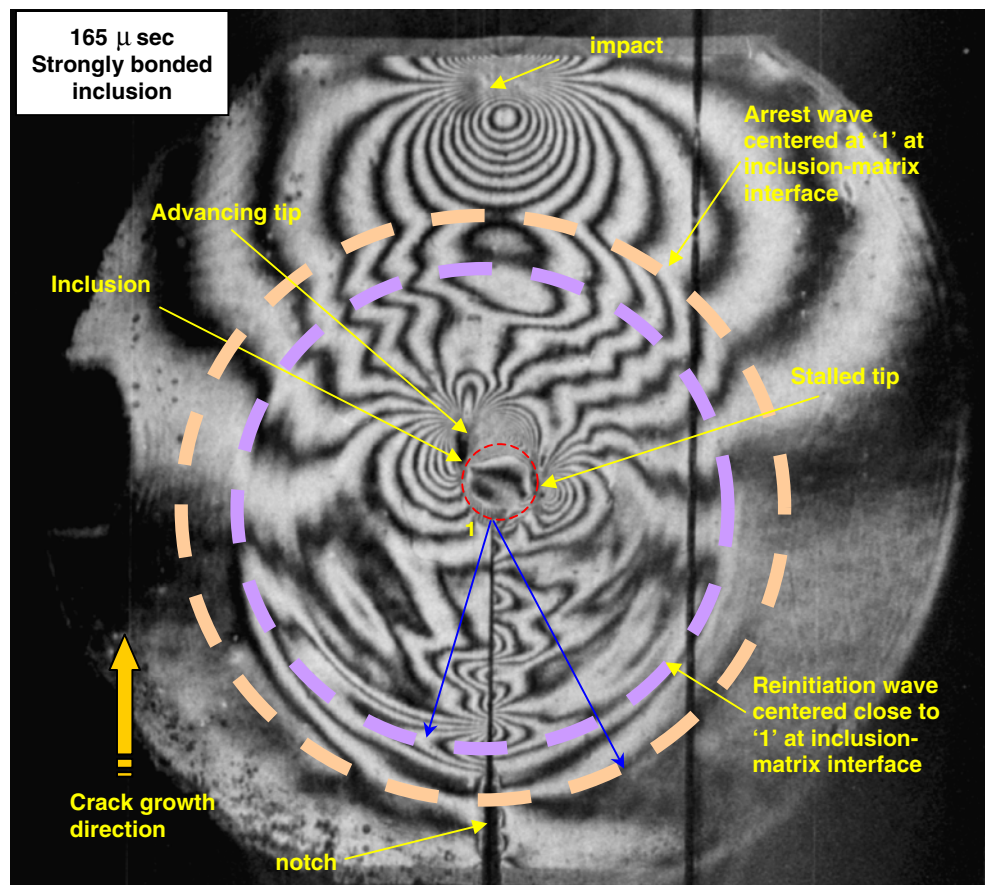


inclusion-matrix interface. On the contrary, when the inclusion is strongly bonded to the matrix, crack path is relatively unaffected [see, Fig. 5(f)]. Similar to the case of $d/2$ eccentricity, mild stress waves (not shown) emerge from weaker inclusion-matrix interface in this case. Interferograms for the strongly bonded case (not shown) on the contrary do not indicate any stress wave generation since the crack-tip does not physically interact with the inclusion located at an offset from the prospective crack path.

The distinct effects of inclusion eccentricity and inclusion-matrix adhesion on crack trajectories can be noticed by comparing images in (Fig. 5). The crack tends to circumvent the strong inclusion-matrix interface in case of all three eccentricities whereas a significant attraction towards the weaker interface is noticed when the inclusion is weakly bonded to the matrix. For all eccentricities the crack lodges into the weaker inclusion-matrix interface and reinitiates from a different location suggesting crack front trapping to be dominant when the inclusion is weakly bonded to the matrix. Stronger inclusion-matrix interfaces, on the other hand, promote crack deflection mechanism. Another interesting observation can be made by comparing crack paths in the vicinity of a weakly bonded inclusion for cases $e=d/2$ and $3d/4$ [see, Fig. 6(c) and (e)]. Even if the

inclusions are located at different offset distances, the crack is attracted towards the interface with nearly the same angle of deflection[3] (~32° for the considered offsets).

## Crack Speed Variations

The interferograms are digitized to determine instantaneous crack length and hence crack speed histories. First, the effect of inclusion eccentricity is described for both weakly and strongly bonded inclusion cases. Note that crack speeds obtained by numerically differentiating crack length history yield an accuracy of about ±25 m/s.

### Effect of Inclusion Eccentricity

The crack speed histories for specimens with weakly and strongly bonded inclusions are shown in Fig. 9(a) and (b), respectively, where plots for all three eccentricities, $e=0$, $d/$

---

[3] The angle a tangent to the crack path at any time instant makes with the original crack orientation direction.
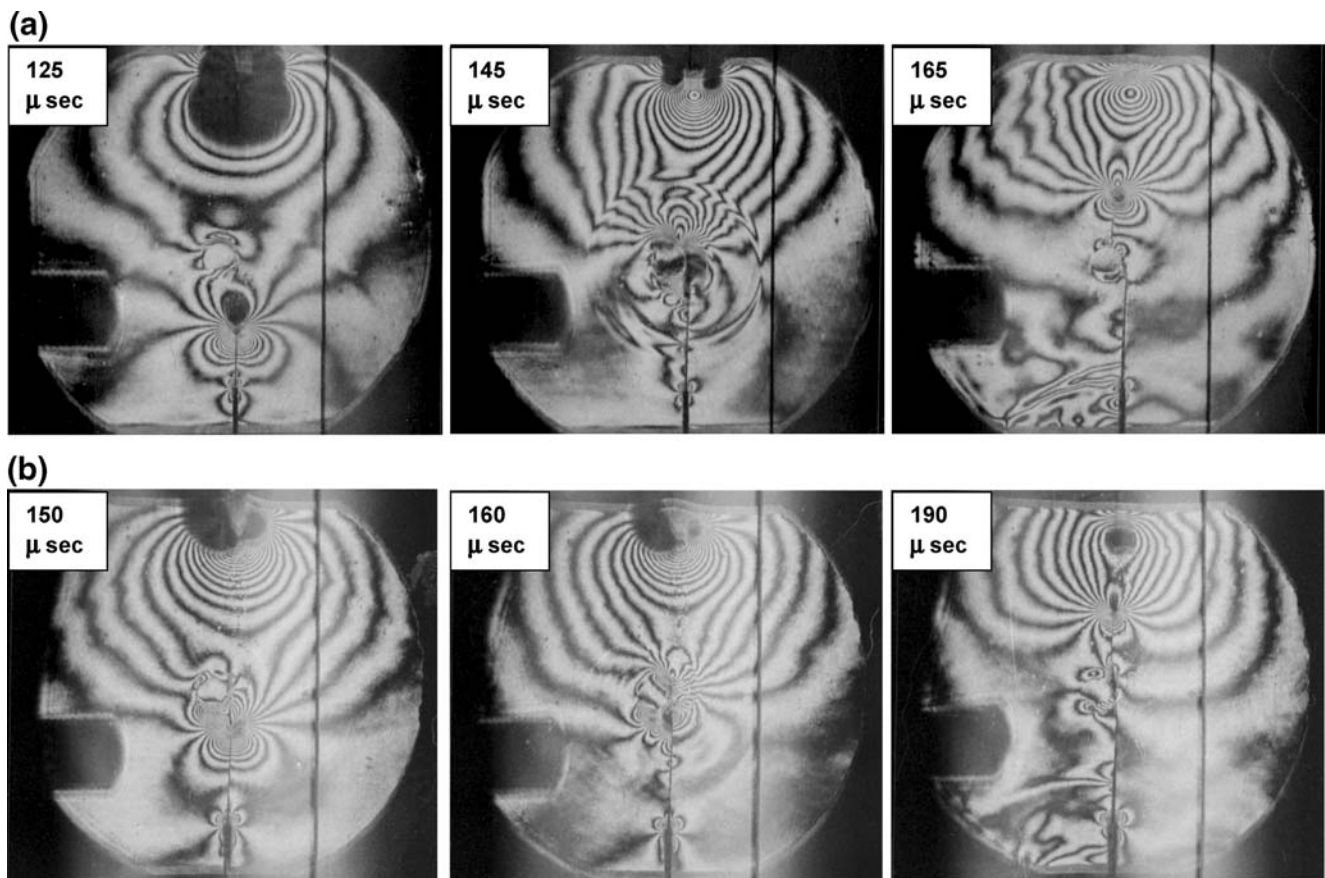
**Fig. 8** Selected fringe pattern representing surface slope contours $\partial w/\partial x$ for epoxy specimen with tangentially located inclusion with respect to initial crack orientation ($e=d/2$). Images show crack-inclusion interaction for the specimen with, (**a**) Weakly bonded inclusion, and (**b**) Strongly bonded inclusion

2 and $3d/4$, are shown. In these, $t_i$ is the time at crack initiation after impact. The crack speed plots in Fig. 9(a) for weakly bonded inclusion cases ($e=0$ and $d/2$) show rapid acceleration ($\sim 10^7$ m/s$^2$) to $\sim 275$ m/s following crack initiation. Subsequently, a small but gradual increase in speed is noticed as the crack approaches the inclusion. Interestingly, these values ($\sim 325$ m/s) just before the crack reaches the inclusion is equal to the mode-I steady-state velocity seen in case of neat epoxy [11]. As the crack encounters the inclusion-matrix interface, both specimens with $e=0$ and $d/2$ show rapid acceleration due to reinitiation from the interface. An extremely high crack speed $\sim 850$ m/s, which is nearly 90% of the Rayleigh wave speed in neat epoxy, at reinitiation is observed.[4] This is due to a combination of high-speed interfacial crack growth (along the weak interface) as well as reinitiation from a 'key-hole' crack front after the crack lodges into the inclusion-matrix

interface. Prior to attaining this peak velocity, a significant drop to $\sim 140$ m/s is seen when the inclusion is located symmetrically ($e=0$). This is an indication of a rapid deceleration, possibly arrest at inclusion-matrix interface, prior to reinitiation. In case of $e=d/2$, however, such a rapid deceleration is not seen as the crack is propagating tangentially to the inclusion. The maximum crack velocity in this case is followed by a drop to $\sim 300$ m/s and subsequently a monotonic reduction prior to total fracture as the crack propagates away from the inclusion towards the impact point. The crack speed variation for $e=3d/4$ is different from the ones for the other two eccentricities. At initiation the crack speed reaches $\sim 350$ m/s. Unlike a gradual increase (after the initial acceleration following crack initiation in $e=0$ and $d/2$ eccentricities), the velocity here ($e=3d/4$) drops gradually to $\sim 200$ m/s. As the crack propagates further and approaches the inclusion, the plot also shows an increasing trend. In the vicinity of the inclusion the crack-tip is attracted towards the weak inclusion-matrix interface and the velocity reaches $\sim 475$ m/s, about half the maximum velocity attained in case of $e=0$ and $d/2$ eccentricities. As the crack propagates away from the inclusion a significant drop followed by a monotonic decrease in velocity is noticed

---

[4] It should be noted that uncertainty in crack speed is rather high during this period due to several transient events, namely, a dominant mode-I crack becoming an interfacial crack before re-emerging as a matrix crack again. The temporal resolution is clearly insufficient to resolve all the details.
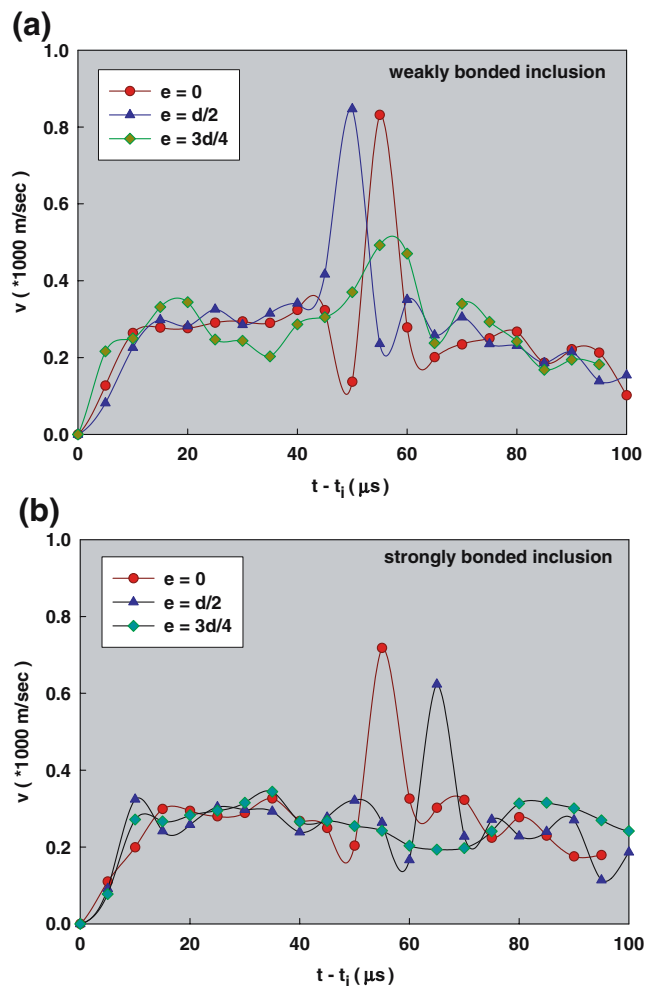
**(a)**



**(b)**



**Fig. 9** Crack velocity histories in specimens embedded with (**a**) weakly bonded and (**b**) strongly bonded cylindrical inclusions. Three different inclusion eccentricities $e=0$, $d/2$ and $e=3d/4$ are considered

similar to the ones seen in case of the other two eccentricities.

Figure 9(b) shows crack speed histories for specimens with strongly bonded inclusions at $e=0$, $d/2$ and $3d/4$ eccentricities. Similar to the weakly bonded inclusion cases, a rapid acceleration (again $\sim 10^7$ m/s$^2$) at crack initiation is seen. As the crack approaches the inclusion, crack speed is $\sim 325$ m/s (approximately equal to the steady-state velocity seen in neat epoxy) before dropping to $\sim 200$ m/s. This deceleration, as the crack approaches the inclusion-matrix interface in case of $e=0$ and $d/2$, is unlike the weakly bonded counterpart where the crack speed increased monotonically until it reached the inclusion-matrix interface. Also, a gradual decrease in velocity is noticed for the case of $e=3d/4$ as the crack approaches the inclusion vicinity. As it propagates past the inclusion, crack speeds reach $\sim 700$ m/s and $\sim 600$ m/sec for $e=0$ and $d/2$, respectively, whereas it continues to decrease to $\sim 200$ m/s for $e=3d/4$ specimen. An instantaneous drop to $\sim 250$ m/s for $e=0$ and $d/2$ and a gradually increasing velocity

to $\sim 300$ m/s for $e=3d/4$ follow next. Subsequently, each specimen fractures completely as the crack propagates away from the inclusion with a monotonically decreasing velocity.

Inclusion-matrix Adhesion Strength Effect

Next, the effect of inclusion-matrix adhesion strength on crack speed is described. In Fig. 10(a) and (b) velocity histories for weakly and strongly bonded inclusions are compared for $e=0$ and $3d/4$ eccentricities, respectively. Figure 10(a) is for the case of a symmetrically located inclusion. The velocity profiles for the weakly and the strongly bonded inclusion cases nearly overlap on each other until the propagating crack approaches the inclusion. Just before reaching the inclusion-matrix interface, the velocity profile for the weakly bonded inclusion deviates from the strongly bonded one. In the former the crack velocity shows a sudden drop to $\sim 140$ m/s (within one 5 μs interval) as the crack reaches the weak inclusion-matrix interface whereas the latter shows a relatively gradual drop from $\sim 300$ to $\sim 200$ m/s in about 15 μs, as the crack propagates and reaches the strong inclusion-matrix interface. Subsequently, reinitiation velocity from the debonded interface in weakly bonded inclusion reaches a rather high value of $\sim 850$ m/s within one interframe period (5 μs), which is $\sim 250\%$ of the steady-state velocity seen in neat epoxy [11]. On the other hand, the deflected crack in the strongly bonded case propagates around the inclusion attaining a somewhat lower maximum velocity of $\sim 700$ m/s. These maximum crack velocities are further followed by a rapid drop to 200 and 300 m/s in weakly and strongly bonded inclusion cases, respectively. The crack speed histories of weakly and strongly bonded cases when the inclusion is located tangentially ($e=d/2$) to the initial crack show features similar to the ones described for $e=0$ and hence a separate description is avoided.

Figure 10(b) shows crack velocity histories of weakly and strongly bonded cases when the inclusion is located at $e=3d/4$ eccentricity. A rapid increase in crack speed at initiation follows a gradual increase to $\sim 375$ m/s in both weakly and strongly bonded cases. As the propagation continues further, the crack speed gradually decreases in case of the strongly bonded inclusion until it reaches a minimum in the inclusion vicinity. On the other hand, the weakly bonded case first shows a decreasing trend before reaching the inclusion followed by an increasing one as the crack meets up with the inclusion-matrix interface. In both specimens the minimum velocity is $\sim 200$ m/s whereas the maximum in the vicinity of the inclusion for weakly bonded case is $\sim 500$ m/s. The crack propagates essentially in the same direction in the vicinity of strongly bonded inclusion whereas the crack reinitiates from the debonded
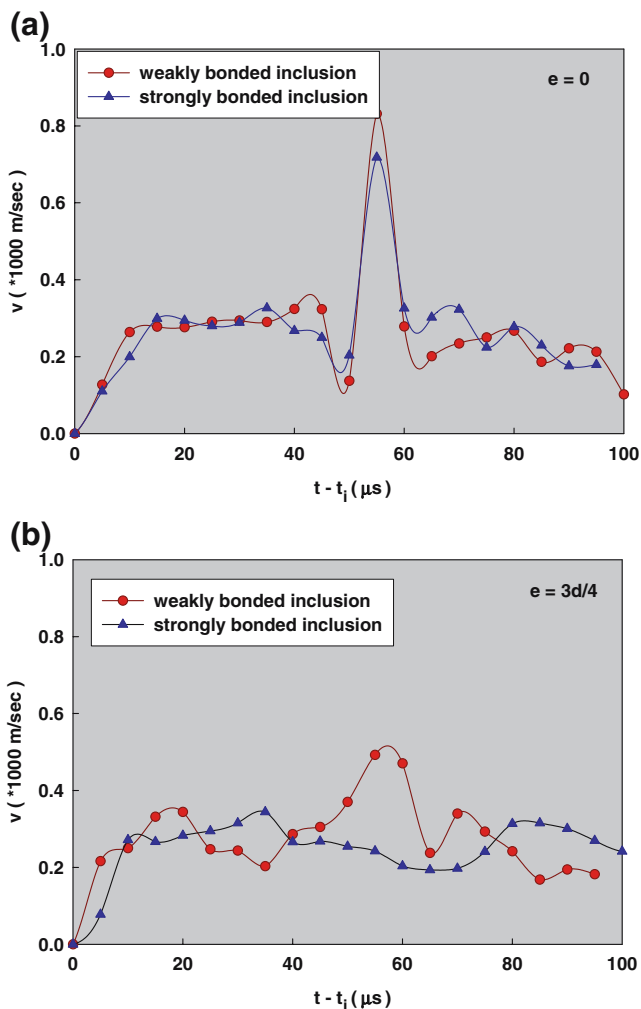
**(a)**



**(b)**



**Fig. 10** Crack velocity histories in epoxy specimen embedded with inclusions, (**a**) symmetrically located ($e=0$) in front of crack-tip, (**b**) located at an offset ($e=3d/4$) to initial crack orientation

inclusion-matrix interface in the specimen with a weakly bonded inclusion. It should be noted that in the weakly bonded inclusion case the propagating crack has deviated from its initial mode-I path towards the inclusion-matrix interface even though the inclusion is not in the prospective crack path and reinitiated at the top of the inclusion-matrix interface at an off-set distance relative to its original path. In case of the strongly bonded inclusion, the crack speed shows an increasing trend for some time as the crack propagates away from the inclusion and then monotonically decreases until the specimen fails completely.

## SIF Variations

As the crack encounters the inclusion, the crack-tip fringes are visibly perturbed by the arrest and reinitiation events. Also, interaction of the crack-tip with the inclusion affects the shape and size of fringes immensely making it difficult

to accurately identify fringe orders. Moreover, when a crack-tip terminates at the inclusion interface, the stress singularity is affected and is different from the one in a monolithic slab [29]. Therefore, fringe analysis using equation (3) becomes difficult and questionable once the crack-tip reaches the inclusion-matrix interface and hence is not attempted in this work. In the following sections, effects of inclusion eccentricity and inclusion-matrix adhesion strength on $K_e$ histories before the crack reaches the inclusion are described. The $K_e$ values are nondimensionalized by the stress intensity factor at crack initiation $(K_e)_i$ in each case. For comparison prominent $K_e$ data are also summarized in Table 1 without non-dimensionalizing. The crack-tip fringes are analyzed only before it reaches the inclusion-matrix interface when the inclusion is in the prospective crack path ($e=0$ and $d/2$). For $e=3d/4$ the fringes are analyzed even after the crack-inclusion interaction and when the crack is propagating away from the inclusion. The fracture behavior of neat epoxy is again considered here as a reference for comparison.[5]

### Effect of Inclusion Eccentricity

Stress intensity factor histories for specimens with weakly and strongly bonded inclusions are shown in Fig. 11(a) and (b), respectively. The weakly bonded inclusions of all three eccentricities in Fig. 11(a) show monotonic increase in $K_e/(K_e)_i$ until the crack initiates from the original tip. The overlapping pre-initiation $K_e/(K_e)_i$ histories suggests the same crack-tip loading rate for all three eccentricities. Also, from the Table 1 it can be seen that $dK_e/dt$ before crack initiation for specimens with an inclusion is close to the one for neat epoxy. The overlapping pre-initiation $K_e$ histories and the same crack-tip loading rate indicate that the inclusion eccentricity does not affect the pre-crack initiation behavior significantly in the cases considered. The crack initiation in each case is followed by a drop in $K_e/(K_e)_i$ before attaining an oscillatory but steady value. A monotonic increase in steady-state $K_e$ with inclusion eccentricity can be seen in Table 1. In each case, post initiation $K_e/(K_e)_i$ histories $(t - t_i > 0)$ shows oscillations about an average value of ~0.8, 0.9 and 1.0 for $e=0$, $d/2$ and $3d/4$ cases, respectively, before the crack-tip meets the inclusion. (The respective steady-state $K_e$ values from Table 1 are ~1.3, 1.5 and 1.8 MPa√m for $e=0$, $d/2$ and $3d/4$, respectively.) The monotonic variation of steady-state $K_e$ with inclusion eccentricity is attributed to the differing effects of stress waves emanating from the impact point on the crack-tip. When the inclusion is symmetrically located ($e=0$), stress

---

[5] The neat epoxy specimen shows an average pre-initiation crack tip loading rate $dK_e/dt \sim 25$ MPa-m$^{1/2}$/msec and the steady state fracture toughness $K_e \sim 1.5$ MPa√m.

**Table 1** The effects of inclusion eccentricity and inclusion-matrix adhesion strength on effective stress intensity factor ($K_e$)

| Inclusion eccentricity ($e$) | Weakly bonded inclusion | | | Strongly bonded inclusion | | |
|---|---|---|---|---|---|---|
| | Pre-initiation crack-tip loading rate $dK_e/dt$ MPa√m/ms | SIF at crack initiation $(K_e)_i$ MPa√m | Effective steady-state SIF $K_e$ MPa√m | Pre-initiation crack-tip loading rate $dK_e/dt$ MPa√m/ms | SIF at crack initiation $(K_e)_i$ MPa√m | Post-initiation crack-tip loading rate $dK_e/dt$ MPa√m/ms |
| 0 | 23 | 1.5 | 1.3 | 23 | 1.47 | 15 |
| $d/2$ | 23 | 1.6 | 1.5 | 24 | 1.54 | 30 |
| $3d/4$ | 23 | 1.75 | 1.8 | 24 | 1.67 | 28 |

The error band on $dK_e/dt$ values is ±3 MPa√m/ms and ±0.1 MPa√m for SIF values.

waves deform the crack-tip in mode-I even after bouncing-off of the inclusion. On the contrary for $e=d/2$ and $3d/4$ stress waves reach the crack-tip in an asymmetric fashion due to their interaction with the inclusion and load the crack-tip in mixed mode (though still mode-I component



(a)

dominates). This results in higher steady-state $K_e$ value for eccentric inclusion cases when compared to the symmetric one. As the crack-tip reaches the proximity of the inclusion, all specimens show a rapid drop in $K_e/(K_e)_i$ values. The effect of crack-inclusion interaction continues even after the crack is propagating away from the inclusion, especially for eccentricities $e=0$ and $d/2$. The $K_e$ values, however, are retrievable only for $e=3d/4$ as the crack-tip fringes are relatively less disturbed in this case. A monotonic drop in $K_e/(K_e)_i$ values are noticeable from the graph prior to complete fracture of the specimen. For the time instants when the crack-tip is at its closest to the inclusion-matrix interface, the interpolated $K_e/(K_e)_i$ values are suggested by a dotted line since crack-tip fringes are difficult to analyze due to emanating stress waves.
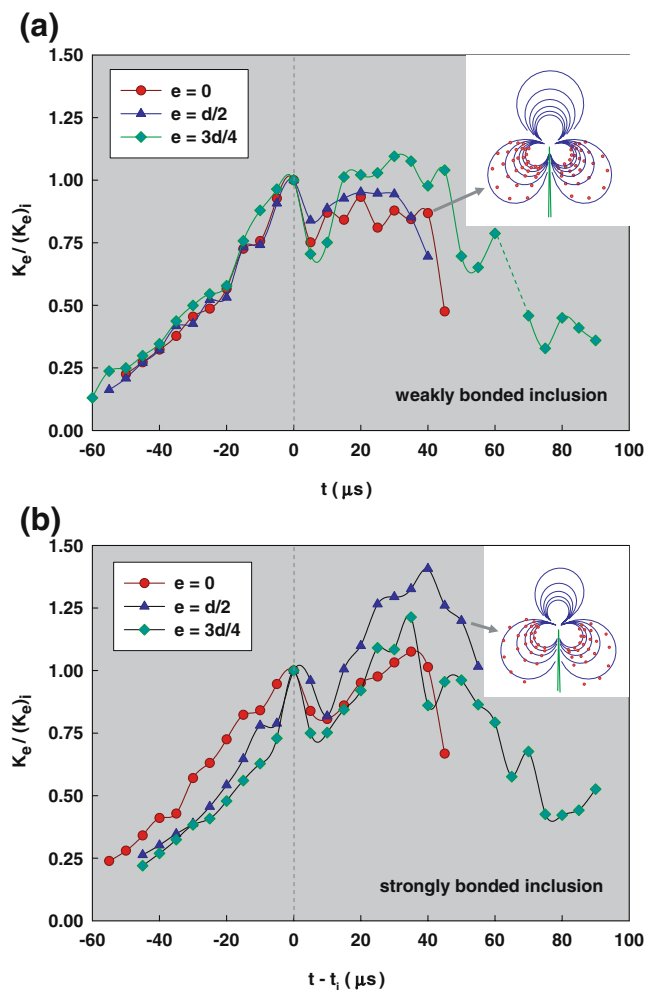
Figure 11(b) shows $K_e/(K_e)_i$ histories for specimens with strongly bonded inclusions. Again, on the average, the rate of increase in $K_e$ is nearly same as that for the weakly bonded case [Fig. 11(a)]. From Table 1 it can be noticed that similar to the weakly bonded inclusion cases, $K_e$ at crack initiation show an increasing trend with inclusion eccentricity. For all eccentricities a dip in $K_e/(K_e)_i$ value at initiation followed by a monotonic increase as the crack-tip approaches the inclusion can be noticed. This is unlike the weakly bonded inclusion cases and is attributed to the reinforcing effect (or, higher matrix constraint) of the strongly bonded inclusion. After initiation ($t - t_i > 0$) the rate of increase in $K_e/(K_e)_i$ depends on inclusion eccentricity. The crack propagates towards the inclusion with a lower $dK_e/dt$ for $e=0$ when compared to the ones for the other two eccentricities. Nearly the same $dK_e/dt$ for $e=d/2$ and $3d/4$ could be viewed as a constant $dK_e/dt$ for a crack propagating towards strongly bonded inclusion as long as the inclusion is near but not in the prospective crack path. When the crack reaches the vicinity of the inclusion a steep drop in $K_e/(K_e)_i$ is seen until it meets the inclusion-matrix interface (for $e=0$) or deviates away from the interface (for $e=d/2$ and $3d/4$). Similar to the weakly bonded inclusion case, a monotonic drop in $K_e/(K_e)_i$ can be noticed for the specimen with strongly bonded inclusion

**Fig. 11** Stress intensity factor histories in specimen embedded with (**a**) weakly bonded and (**b**) strongly bonded cylindrical inclusions. Insets in (**a**) and (**b**) show the quality of least-square fits of digitized data in weakly and strongly bonded cases when the crack is in the proximity of the inclusion

at $3d/4$ eccentricity as the crack propagates away from the inclusion. As mentioned earlier, for $e=0$ and $d/2$ the fringes could not be analyzed due to post crack-inclusion interaction transients. The insets in Fig. 11(a) and (b) show the quality of the least-square fits of the digitized data used in the analysis. The fits shown in the figures are for the specimens with weakly ($e=0$ at 135 μs) and strongly ($e=d/2$ at 150 μs) bonded inclusions. The high-quality fits suggest the accuracy of the calculations and robustness of the method even when the tip is relatively close to the inclusion.

### Effect of Inclusion-matrix Adhesion Strength

Next, the effect of bond strength between an inclusion and the matrix on SIF is discussed. Figure 12(a) shows $K_e/(K_e)_i$ histories of weakly and strongly bonded inclusions at $e=0$ eccentricity. Both show nearly same pre-initiation behaviors ($dK_e/dt \sim 23$ MPa$\sqrt{m}$/ms, see, Table 1). After a dip in $K_e/(K_e)_i$ following crack initiation, as the crack propagates towards the inclusion, SIF values oscillate about an average in case of the weakly bonded inclusion. On the other hand, in case of the strongly bonded inclusion, a monotonic increase in $K_e/(K_e)_i$ is seen. In the close proximity of the inclusion, both show a steep drop in $K_e/(K_e)_i$ with nearly the same rate. The comparison of $K_e$ histories of the weakly and the strongly bonded cases when the inclusion is located tangentially ($e=d/2$) to the initial crack orientation show features similar to the ones for $e=0$ and therefore a detailed description is avoided. The $K_e$ profiles for $e=d/2$ show higher crack initiation and steady-state $K_e$ values (for the weakly bonded inclusion) and higher $dK_e/dt$ (for the strongly bonded inclusion) when compared to the ones for $e=0$.

Figure 12(b) shows the effect of inclusion-matrix adhesion strength when the inclusion is located at an offset of $e=3d/4$ to the initial crack orientation. Again, similar pre-initiation behavior with nearly the same crack-tip loading rate is noticed for both the weakly and strongly bonded inclusion cases. The crack initiated at nearly the same $K_e$ values ($\approx 1.75$ and 1.67 MPa$\sqrt{m}$ in weakly and strongly bonded inclusions, respectively (see, Table 1)). Similar to $e=0$, the crack growth in the specimen with a weakly bonded inclusion at $e=3d/4$ stabilizes when the crack propagates towards the inclusion but at a relatively higher $K_e/(K_e)_i$ whereas in case of the strongly bonded counterpart, the crack grows towards inclusion with a monotonically increasing $K_e/(K_e)_i$. Both the weakly and strongly bonded inclusions show a rapid drop in $K_e/(K_e)_i$ value followed by a monotic drop in $K_e/(K_e)_i$ as the crack propagates away from the inclusion.

The inclusion-matrix adhesion strength effect on mode-mixity (phase angle, $\psi$) is described next. The variation of mode-mixity with $t-t_i$ is plotted in Fig. 13 for the weakly
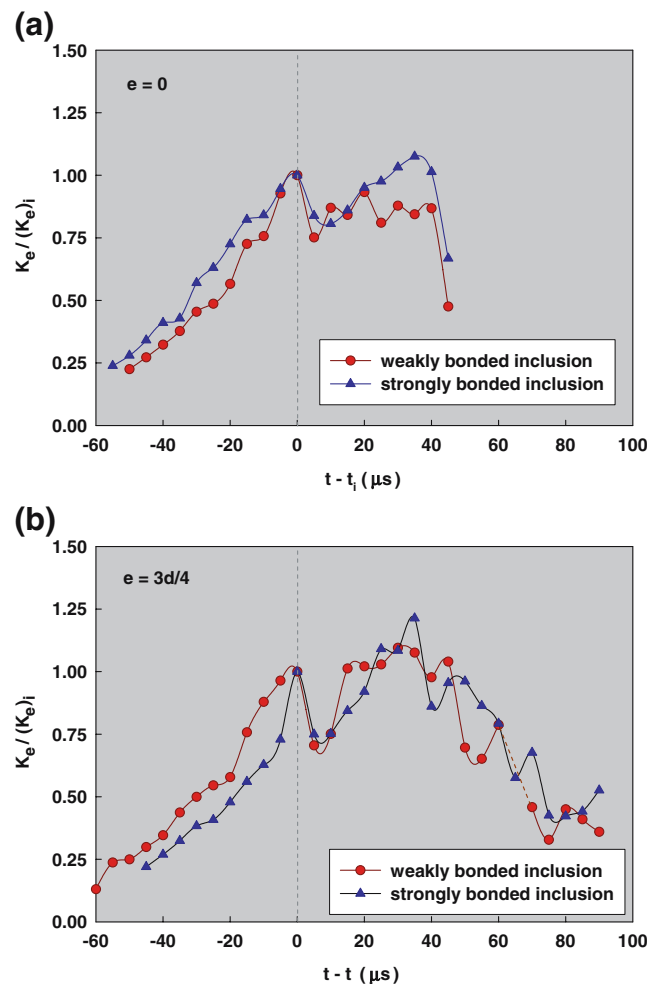


**Fig. 12** Stress intensity factor histories in specimen embedded with cylindrical inclusions, (**a**) inclusion is symmetrically located ($e=0$) in front of the crack-tip, (**b**) inclusion is located at an offset ($e=3d/4$) to initial crack orientation

and strongly bonded inclusion cases of $e=3d/4$ eccentricity. The crack-tip fringes are analyzed here even after the crack grows past the inclusion (except for the time instant 65 μs after the initiation from the original tip in weakly bonded case which is represented by an interpolated dotted line). At crack initiation mode-II stress intensity factor ($K_{II}$) is nearly zero and the crack travels in mode-I for ~40 μs after initiation in both weakly and strongly bonded inclusion specimens. As the crack gets close to the inclusion, significantly different mode-mixities evolve in the two cases. Following a small positive mode-mixity for about 15 μs, $\psi$ becomes negative in the strongly bonded inclusion specimen. This is consistent with the crack trajectory shown in the Fig. 5(f) where the crack deviates away from the inclusion after being slightly attracted towards the inclusion. The absolute value of the angle $\psi$ tends to decrease after attaining a value of ~30°. Contrary to the strongly bonded case the positive mode-mixity continues to increase in case of the weakly bonded inclusion specimen until it
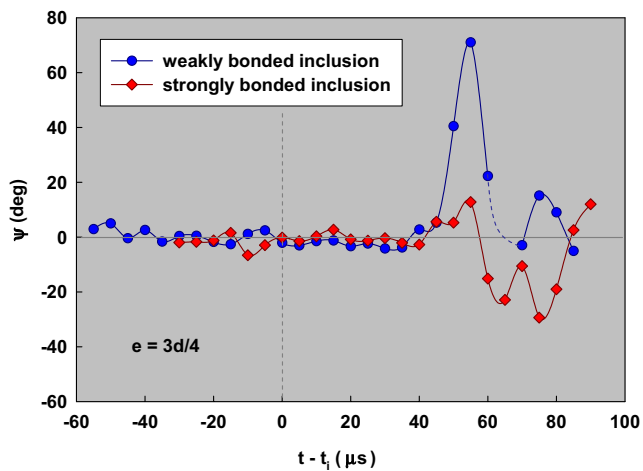
**Fig. 13** Variation of mode-mixity ($\psi = \tan^{-1} (K_{II}/K_{I})$) for weakly and strongly bonded inclusions at $3d/4$ eccentricity

reaches a maximum value of $\sim 70°$. This indicates a strong attraction of the crack-tip by the weak interface. This also suggests that the crack requires significantly higher energy to propagate in the presence of weakly bonded inclusion when compared to the strongly bonded one. Also, the opposite mode-mixities in the two cases are consistent with the crack being attracted towards inclusion in one case [see, Fig. 5(e)] whereas it is repelled away in the other [Fig. 5(f)]. Once the crack grows past the inclusion, mode-mixities tend to become zero in both weakly and strongly bonded inclusion specimens.

## Discussion

The experimental results show significantly different crack-inclusion interaction behaviors for different inclusion-matrix interface strengths. The crack deflection mechanism dominates when the inclusion is strongly bonded to the matrix. However, the crack is attracted towards and often lodges into a weaker inclusion-matrix interface for cases with smaller eccentricities. The associated localized blunting (or, the so-called 'key-holing' effect) of the crack front temporarily retards growth, possibly arresting it momentarily.[6] The reinitiation of the crack in this case involves relatively higher crack velocities and velocity gyrations. Hence greater energy dissipation occurs in case of weakly

bonded inclusion when compared to the strongly bonded one as the crack front deflects around the inclusion relatively smoothly. Other differences in toughening mechanisms can be identified by examining fracture surfaces in these two cases. In Fig. 14, micrographs from regions close to the inclusion (within 2 mm) before and after the crack approaches and recedes from the crack-inclusion interface are shown for the case of zero eccentricity ($e=0$). The fracture surfaces just before the crack encounters the inclusion in both weakly and strongly bonded inclusion specimens show a river-bed pattern. In the former, however, tail lines are also interspersed within the river-bed morphology. The occurrence of tail lines are an indication of surface tortuosity due to crack front twisting during the fracture process and suggests the presence of a mode-III component locally [12]. The difference between fracture surfaces of weakly and strongly bonded inclusion cases is much more distinct in images from regions [see Fig. 14(c) and (d)] where the crack front is receding from the inclusion. Presence of a large number of tail lines suggest a rather high energy dissipation in weakly bonded case due to reinitiation from a momentarily arrested crack front whereas very few tail lines in strongly bonded inclusion case indicates comparatively smoother crack propagation.

It is also interesting to compare the observations of the current work with the previous ones by the authors on dynamic fracture behavior of glass-filled epoxy [11, 12, 30] particulate composite systems. A systematic study conducted on samples with solid spherical filler particles of various sizes (7–200 μm) but identical volume fraction have shown that macroscopic steady-state fracture toughness is consistently higher when the filler is bonded weakly to the matrix compared to the ones that are strongly bonded [11]. (The bell shaped variation of steady-state fracture toughness with particle size in this work has also suggested an optimum particle size for a given volume fraction.) In [12], the authors have also shown that higher fracture toughness can be linked to higher microscopic fracture surface roughness even in particulate composites. They have identified a roughness parameter namely 'fracture induced roughness—$R_f$,' a fraction of the total surface roughness, that correlates with the stead-state fracture toughness. The optical and microscopic evidence presented in the current work explain the observations reported in [11, 12]. The loading rate effects demonstrated on this particle filled polymer system is demonstrated in [30] by comparing steady-state fracture toughness values with the ones obtained under quasi-static loading conditions for various filler particle sizes at a fixed 10% volume fraction. Although bell shaped variations are observed in both cases, loading rate effects are shown to produce a complex fracture toughness response depending upon the average particle size. At the optimum particle size, the steady-state

---

[6] The crack-inclusion interaction behavior is numerically studied in recent years [17, 18, 20] under quasi-static conditions. These investigations have also noted that a crack deflects around a strongly bonded inclusion whereas an inclusion-matrix interface with a pre-existing debond attracts the propagating crack. Apart from this qualitative similarity, however, numerical models cannot be directly compared with the current experimental observations due to the presence of inertial effects and matrix constraint due to multiple interacting inclusions along the crack front.

**Fig. 14** Crack surface (x–z plane) features in the vicinity (<2 mm) of inclusions for the case $e=0$. The arrows denote the direction of crack propagation. (**a**), (**b**)—fracture surfaces just before reaching the inclusion-matrix interface in weakly and strongly bonded inclusion cases, respectively. The features of inclusion-matrix interface can be seen at the top of each image. (**c**), (**d**)—fracture surfaces in weakly and strongly bonded specimens, respectively, when the crack is propagating away from the inclusion. Note the higher frequency of trail-lines and higher surface roughness in the weakly bonded inclusion case (micrographs (**a**) and (**c**))
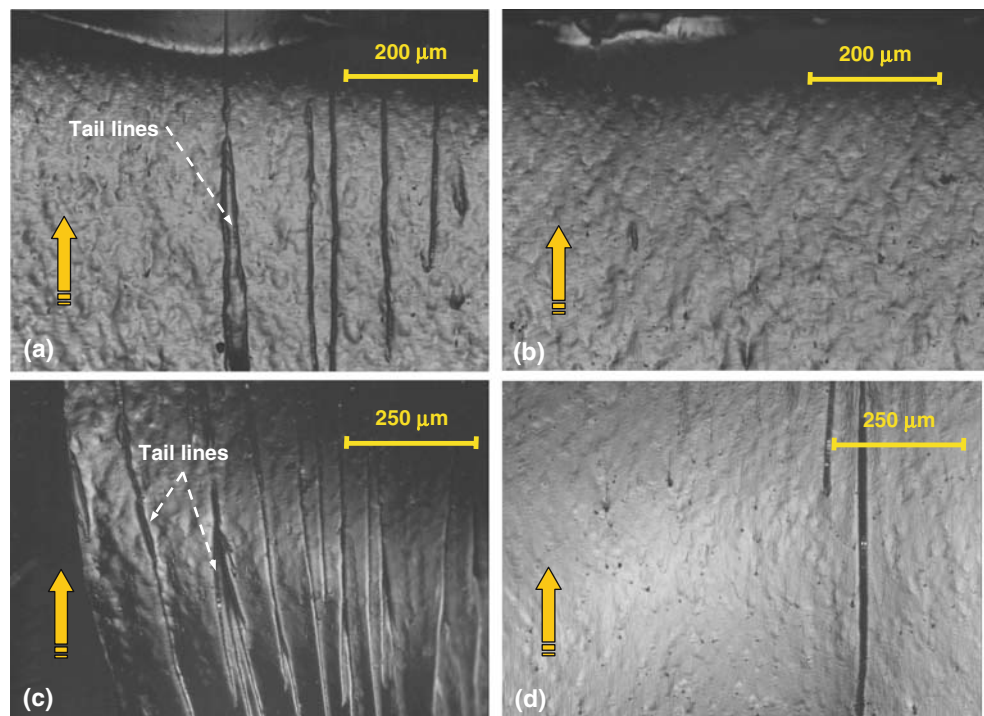


stress intensity factor under dynamic conditions is lower than the one under static loading conditions.

## Conclusions

To understand the fundamental toughening mechanisms involved in heterogeneous materials investigations on crack-particle interactions are carried out using optical interferometry and high-speed photography. The test specimens are prepared using two types of cylindrical glass inclusions, strongly and weakly bonded to the matrix epoxy and located at three different eccentricities, symmetrically ($e=0$), tangentially ($e=d/2$) and at an offset ($e=3d/4$) with respect to the initial crack plane.

Fractured specimens show distinct crack trajectories in each case. A weaker inclusion-matrix interface attracts the propagating crack whereas a stronger interface deflects the crack away. The crack-inclusion interactions produce multiple stress waves. The arrest and reinitiation waves are concentric in case of the strongly bonded inclusion suggesting origination of arrest and reinitiation waves from relatively close spatial positions with a time delay between the two events. The same waves seem to be of nearly same size but spatially shifted in the weakly bonded inclusion case. This implies origination of the two waves from different locations on the interface with a spontaneous (compared to the time resolution used in this work) debonding of the weak interface. This examined in conjunction with crack paths from fractured specimens indicates two different failure mechanisms, crack deflection

and crack-front 'key-holing,' respectively, for strongly and weakly bonded inclusion specimens.

For all cases considered, crack velocities near inclusions are affected by inclusion eccentricity and inclusion-matrix adhesion strength. When an inclusion is in the prospective crack path, the crack speed is higher in the weakly bonded case approaching the Rayleigh wave speed for the matrix material. The effect of the inclusion on the crack speed is small when the crack is not in the proximity of the inclusion. For the cases when the inclusion is not in the prospective crack path, relatively less variation in crack velocity is seen. However, the presence of the inclusion is felt more by a propagating crack when the inclusion is weakly bonded to the matrix.

Measurable inclusion eccentricity and inclusion-matrix adhesion strength effects exist on fracture parameters as well. For all cases considered, similar pre-initiation behaviors including similar crack-tip loading rates are noticed. For both weakly and strongly bonded cases $K_e$ at crack initiation shows a small but monotonic increase in magnitude with inclusion eccentricity. For a crack propagating towards a weakly bonded inclusion, an effective stress intensity factor ($K_e$) value stabilizes to a constant value for each inclusion eccentricity. The $K_e$ values drop instantaneously when the crack-tip is very close to the inclusion and meets up with weak/weakened inclusion-matrix interface. The steady value of $K_e$ in the steady-state zone increases with increasing inclusion eccentricity. On the other hand, the strongly bonded inclusion cases show monotonically increasing $K_e$ as cracks propagate towards the inclusion. Following crack-inclusion interaction $K_e$

decreases monotonically until the specimen fractures in both weakly and strongly bonded inclusion cases of all eccentricities. The opposite signs of mode-mixities suggest crack attraction towards weaker inclusion-matrix interfaces and repulsion from stronger interfaces, respectively. The absolute maximum mode-mixity when the inclusion is weakly bonded to the matrix is more than twice that of the strongly bonded case, suggesting greater resistance to crack propagation in case of weakly bonded interfaces compared to the strongly bonded counterparts.

# References

1. Frear DR (1999) Materials issues in area-array microelectronic packaging. J Met 51(3):22–27.
2. Yazici R, Karuv B, Garrow J, Kalyon DM (1999) Particulate based conductive composites exploiting percolation-range microstructure. Soc. Plastics Engineers, Annual Technical Conference, Technical papers, 45, 1551–1555.
3. Kessler MR, Sottos NR, White SR (2003) Self-healing structural composite materials. Compos A 34:743–753.
4. Brown EN, Sottos NR, White SR (2002) Fracture testing of a self-healing polymer composite. Exp Mech 42(4):372–379.
5. Norman SA, Michele E, Amaya A, Gonzalo S, Christopher ML, Verran J, Stratton J, McIntyre RB (2004) Degradation and stabilization of polymers and coatings: nano versus pigmentary titania particles. Polym Degrad Stab 85:927–946.
6. Seamark MJ (1991) Use of syntactic foams for subsea buoyancy. Cell Polym 10(4):308–321.
7. Thomas CR (1973) Invited review: syntactic carbon foam. Mater Sci Eng 12(5–6):219–233.
8. Hiel C, Dittman D, Ishai O (1993) Composite sandwich construction with syntactic foam core: a practical assessment of post-impact damage and residual strength. Composites 24(5):447–450.
9. Gdoutos EE, Pilakoutas K, Rodopoulos CA (2000) Failure analysis of industrial composite materials. McGraw-Hill, New York, pp 533–540.
10. Butcher RJ, Rousseau CE, Tippur HV (1998) A functionally graded particulate composite: preparation, measurements and failure analysis. Acta Mater 47(1):259–268.
11. Kitey R, Tippur HV (2005) Role of particle size and filler-matrix adhesion on dynamic fracture of glass-filled epoxy, I. Macro-measurements. Acta Mater 53:1153–1165.
12. Kitey R, Tippur HV (2005) Role of particle size and filler-matrix adhesion on dynamic fracture of glass-filled epoxy, II. Linkage between macro- and micro-measurements. Acta Mater 53:1167–1178.
13. Tamate O (1968) The effect of a circular inclusion on the stresses around a line crack in a sheet under tension. Int J Fract 4:257–265.
14. Atkinson C (1972) The interaction between a crack and an inclusion. Int J Eng Sci 10:127–136.
15. Erdogan C, Gupta GD, Ratwani M (1974) Interaction between a circular inclusion and an arbitrary oriented crack. J Appl Mech (Transaction of the ASME) 41:1007–1013.
16. Gdoutos EE (1985) Stable growth of a crack interacting with a circular inclusion. Theo App Fract Mech 3:141–150.
17. Li R, Chudnovsky A (1993) Variation of the energy release rate as a crack approaches and passes through an elastic inclusion. Int J Fract 59:R69–R74.
18. Bush MB (1997) The interaction between a crack and a particle cluster. Int J Fract 88:215–232.
19. Knight MG, Wrobel LC, Henshall JL, De Lacerda LA (2002) A study of the interaction between a propagating crack and an uncoated/coated elastic inclusion using the BE technique. Int J Fract 114:47–61.
20. Kitey R, Phan A-V, Tippur HV, Kaplan T (2006) Modeling of crack growth through particulate clusters in brittle matrix by symmetric-Galerkin boundary element method. Int J Fract 141 (1–2):11–25.
21. Lei J, Wang Y-S, Gross D (2005) Analysis of dynamic interaction between an inclusion and a nearby moving crack by BEM. Eng Anal Bound Elem 29:802–813.
22. O'Toole BJ, Santare MH (1990) Photoelastic investigation of crack-inclusion interaction. Exp Mech 30(3):253–257.
23. Tippur HV (1994) Interpretation of fringes obtained with coherent gradient sensing. Appl Opt 33(19):4167–4170.
24. Tippur HV (1992) Coherent gradient sensing: a Fourier optics analysis and application to fracture. Appl Opt 31(22):4428–4439.
25. Krishnaswamy S, Tippur HV, Rosakis AJ (1992) Measurements of transient crack-tip deformation fields using the method of coherent gradient sensing. J Mech Phys Solids 40(2):339–372.
26. Tippur HV, Krishnaswamy S, Rosakis AJ (1991) Optical mapping of crack-tip deformations using the methods of transmission and reflection coherent gradient sensing: a study of crack tip $K$-dominance. Int J Fract 52:91–117.
27. Vaziri A, Nayeb-Hashemi H (2005) The effect of crack surface interaction on the stress intensity factor in mode III crack growth in round shafts. Eng Fract Mech 72:617–629.
28. Gross TS (1988) On the effect of face contact and friction due to fracture surface roughness in edge cracks subjected to external shear. Eng Fract Mech 31(3):405–420.
29. Freund LB (1990) Dynamic fracture mechanics. Cambridge University Press, Cambridge, UK.
30. Kitey R, Tippur HV (2005) Dynamic crack growth in particulate bimateials having discrete and diffuse and diffuse interfaces: role of microstructure. Eng Fract Mech 72:2721–2743.